Acta Materialia, Volume 234, August 2022, Article number 118033
DOI: 10.1016/j.actamat.2022.118033

Friction-induced phase transformations and evolution of microstructure of austenitic stainless steel observed by operando synchrotron X-ray diffraction

K. Emurlaev[a,*], I. Bataev[a], I. Ivanov[a], D. Lazurenko[a], V. Burov[a], A. Ruktuev[a], D. Ivanov[b,c,d], M. Rosenthal[e], M. Burghammer[e], K. Georgarakis[f], A.M. Jorge Junior[g,h,i]

[a]Faculty of Mechanical Engineering and Technologies,Novosibirsk State Technical University, Karl Marks av. 20, Novosibirsk, 630073, Russian Federation
[b]Institut de Sciences des Matériaux de Mulhouse-IS2M, CNRS UMR 7361, F-68057 Mulhouse, France
[c]Faculty of Chemistry, Lomonosov Moscow State University (MSU), GSP-1, 1-3 Leninskiye Gory, 119991 Moscow, Russian Federation
[d]Institute of Problems of Chemical Physics, Russian Academy of Sciences, Chernogolovka, Moscow region, 142432, Russian Federation
[e]European Synchrotron Radiation Facility, F-38043 Grenoble, France
[f]School of Aerospace, Transport and Manufacturing, Cranfield University, Cranfield MK43 0AL, UK
[g]Federal University of São Carlos, Via Washington Luiz, Km 235, 13565-905 Sao Carlos, SP, Brazil
[h]Université Grenoble Alpes, Université Savoie Mont Blanc, CNRS, Grenoble INP, LEPMI, 38000 Grenoble, France
[i]Université Grenoble Alpes, CNRS, Grenoble INP, SIMAP, 38000 Grenoble, France

Abstract

A materials' structure and its evolution due to friction play a crucial role in understanding wear and related processes. So far, structural changes caused by friction are mostly studied using ex situ destructive characterization techniques, such as microscopy of post-mortem the prepared specimen by polishing and etching techniques. In this paper, the structural changes of AISI 321 austenitic stainless steel (ASS) during frictional loading were observed by the nondestructive operando method based on synchrotron X-ray diffraction (XRD). Although the martensitic transformation in AISI 321 steel starts at ca. -187 °C, frictional loading induces γ-(ε, α′) transformation in this alloy at room or even higher temperatures. The ε-martensite formation is observed only for a relatively short time. Subsequently, a mechanically mixed layer (MML), composed mainly of the α′ phase, forms at the sample's surface. Using XRD peak profile analysis, we observed the accumulation of dislocations, their ordering, and/or stress field shielding before and after phase transformations. The steady-state conditions are reached after ca. 69 friction cycles manifested in reaching the threshold values of the size of the coherent scattering regions (CSR) and dislocation density in γ and α′ phases. For a better understanding of structural evolution, the microstructure of the sample was studied by scanning electron microscopy (SEM) after the experiment. The structure of the MML, its delamination, the formation of vortices, and carbide crushing are discussed.

Keywords: austenitic stainless steel, friction, synchrotron X-ray diffraction, operando, peak profile analysis

1. Introduction

Austenitic stainless steels (ASSs) possess a good combination of mechanical and technological properties and high corrosion resistance in various environments. For these reasons, ASSs have found wide applications in different manufacturing fields, particularly in mechanical engineering, aerospace engineering, and chemical engineering. Products made of ASSs are frequently subjected to cyclic loading. At low temperatures, the cyclic loading of ASS can lead to strain hardening through a strain-induced phase transition, during which metastable austenite (γ) transforms to martensite (α′ or ε), also known as mechanically or strain-induced martensite [1]. A brief overview of strain-induced transformations in ASSs can be found in Supplementary Material 1.

*Corresponding author.
Email address: emurlaev@corp.nstu.ru (K. Emurlaev)

Published by Elsevier. This is the Author Accepted Manuscript issued with: Creative Commons Attribution Non-Commercial No Derivatives License (CC:BY:NC:ND 4.0).
The final published version (version of record) is available online at DOI:10.1016/j.actamat.2022.118033. Please refer to any applicable publisher terms of use.

The formation of mechanically induced martensite is also frequently observed during abrasive wear [2, 3] and sliding friction [4, 5, 6, 7, 8]. With adequately selected friction conditions, this phenomenon can be used as a finishing treatment to obtain products with low surface roughness and high mechanical properties [9, 10]. The reasons for the formation of friction-induced martensite are high specific stresses and strains resulting from the adhesive-cohesive interaction between the materials of the friction pair [11, 12], as well as the indentation of wear debris in the surface of the material, which leads to high local strains [12, 13].

The structural evolution of materials during friction is manifested in grain refinement, rotation of grains and their alignment in the sliding direction, crystallographic texturing, change of the dislocation structure, and the formation of a mechanically mixed layer (MML), also known as "third body" or transfer layer. Strain-induced martensite also forms at some stage of friction, exerting significant influence on other processes of structural transformation caused by friction.

The ASS structure, formed due to friction, has been investigated in many works [4, 5, 6, 7, 8]. However, most of them used post-mortem analysis of the samples. In other words, the analysis was usually carried out using destructive characterization techniques providing information on the structural state and phase constitution of the sample's surface layer only at a specific time. However, the entire sequence of transformations, leading to the formation of the final structure remained unclear. For instance, the mechanism of friction-induced martensite formation and the moment when this occurs have not yet been clarified.

It can be noticed that most studies devoted to diffusionless transformations are based on microstructural investigations conducted after the experiment (i.e., ex situ). Friction experiments are not an exception as it is quite challenging to design and perform in situ observations in practice. Nevertheless, examples of such experiments do exist. For instance, back in the 1980s and 1990s, the friction experiments were carried out with simultaneous observation using scanning electron microscopy (SEM) and scanning Kelvin probe microscopy, aiming to analyze changes in the surface structure and its chemical composition during the tests [4], [14, 15]. Recently, Rowe et al. [16] and Yagi et al. [17] developed an approach that allows the measurement of the temperature at the friction interface using the thermography method. The temperature can also be measured by Raman spectroscopy [18]. The wear behavior can be analyzed by recording acoustic emission generated by the propagation of elastic deformation waves [19]. Indeed, measuring the friction coefficient is also an in situ observation of friction interaction. All these approaches, however, are insufficient to fully understand the response of the microstructure to friction.

An in situ approach using synchrotron X-ray diffraction (XRD) to investigate the material state under sliding was recently proposed in [17, 20, 21]. Using the combination of synchrotron radiation (SR) and two-dimensional detectors, one can record high-quality diffraction patterns with high spatiotemporal resolution. The application of such methods provides a possibility to probe the material state under different friction conditions and obtain diffraction patterns directly during the experiment/operation with a high sampling rate, that is, to implement in situ or operando observations. Yagi et al. [17, 22] and Izumi et al. [21] used such an approach coupled with temperature measurements to identify the formation of austenite during the dry sliding of steel with a martensitic structure. They also observed that full width at half maximum (FWHM) of the martensite peaks decreases, indicating a decrease in the number of crystal structure defects due to recovery and recrystallization of the alloy. In addition, using diffraction analysis, Yagi et al. [17] assessed the fraction of martensite and austenite phases, which is important for analyzing the dynamics of friction-induced phase transformations.

The development of diffraction methods for the characterization of materials' structure during friction poses a new challenge for tribologists – the assessment of the dislocation structure dynamics. In recent decades, several novel peak profile models have been proposed, namely, the so-called modified Williamson-Hall (MWH) and modified Warren-Averbach (MWA) methods [23, 24]. These methods are based on the Krivoglaz theory [25] of the effect of dislocations on the elastic strains and adequately address the effect of the anisotropy of the sample's elastic properties on diffraction peak profiles. In contrast to the conventional Williamson-Hall and Warren-Averbach methods, these modified methods allow calculations of not only the size of the coherent scattering regions (CSRs) but also the dislocation density, the relative distribution of dislocations by type (or by slip systems), and other parameters of the microstructure [23, 26, 27]. We believe that it is possible to extract unique data on the friction and related processes using MWA and MWH models coupled with an in situ or operando XRD experiment.

Recently, Bataev et al. [28] used MWH and MWA methods and proposed an operando approach to analyze the structural evolution of materials under friction using synchrotron XRD. Until now, this approach was used only for relatively simple materials (e.g., carbon steel) that do not experience friction-induced phase transformations. In the

case of γ-α' transformation in ASSs, the dislocation pile-ups become sites of α'-martensite nucleation. For this reason, we believe that considering of dislocation dynamics during the friction of ASSs is an essential issue. Only by properly addressing this fundamental issue can the effect of mechanically induced transformation on tribological properties of ASSs and the transition from mild to catastrophic wear be clarified.

2. Experimental procedure

2.1. Operando observation and sample preparation

The sliding test was carried out in pin-on-disk geometry using the friction tester described previously [28, 29]. The experimental setup is shown schematically in Fig. 1. This scheme implies that each point at the sample surface was subjected to cyclic frictional loading. The whole experiment consisted of 500 revolutions of the sample (or friction cycles). During the friction test, the surface layer of the sample was probed by a micron-sized X-ray beam in grazing incidence diffraction geometry with a grazing angle of 3.4°. Before the experiment, the disk-shaped sample was pressed against a rigidly fixed pin with a weight of 16 kg. The whole tester with the sample was then positioned carefully relative to the X-ray beam to probe the friction surface at a distance of approximately 3 mm behind the pin. Ideally, the distance between the beam and the pin should be as small as possible. However, in this case, the pin absorbs the part of the diffraction cones. Due to this reason, the distance between the pin and the beam was set to 3 mm. We believe that there are no significant differences in the diffraction patterns recorded at the distance of 3 mm or at any other distance from the pin since the structure of the surface doesn't significantly change when the material comes out of the friction zone. This statement is correct except in the case of dramatic friction-induced heating. Considering the angular velocity (60 rpm) and the disk diameter (66 mm), the time taken from the pin's contact with a region on the sample's surface to the acquisition of the diffraction pattern from this region was calculated to be less than 0.015 s. The friction regime was selected based on our previous experience to satisfy the following conditions [28] . First, we tried to minimize the effect of the radial runout. Due to the slight misalignment of the sample's and the spindle's axes, the point of incidence of the X-ray beam can move on the friction surface when the sample is rotated. Although such movement is only of the order of a few micrometers, it nevertheless slightly affects the sample-to-detector distance, resulting in the peak broadening. By the trial-and-error method it was found that at a rotation frequency of 60 rpm and below the effect of sample's radial runout doesn't affect the shape of XRD peaks, since the acquisition time is short enough to neglect the slow radial motion of the sample. Secondly, we tried to achieve regimes when the damage of the friction surface occurred gradually without significant changes in the very first friction cycles. Thirdly, we tried to avoid significant heating in the zone of contact between the pin and the sample. This was especially important for our study, as we could not measure the heating caused by friction and make appropriate corrections in the subsequent calculations. According to our estimates, friction can cause a temperature increase of up to 172 °C. Calculation procedure is briefly described in Supplementary material 2 and in studies [30, 31, 32]. It should be noted that heat dissipation due to radiation and convection were not taken into account. It means that the actual temperature at the interface can be significantly lower.

Thus, the operando approach to study friction-induced structural evolution was implemented. Scattered radiation was collected using an exposure time of 5 ms at a sampling rate of 100 frames per minute by means of a photon-counting area detector (EigerX 4M from Dectris). The active area of the detector is 162.5×155.2 mm^2, the resolution 2070×2167 pixels, and the pixel size 75×75 μm^2. The monochromatic X-ray beam with a photon energy of 13.9 keV was focused by means of a compound refractive Be-lens optics to a nominal beam size of 1.3×2.8 μm^2 (vertically and horizontally, respectively) at the sample position. The beam's footprint on the work surface of the sample was 22×2.8 μm^2 because of the grazing incidence geometry. The grazing incidence geometry was achieved by tilting the entire friction device. This approach allows analyzing thin surface layers of the sample as the penetration depth of the X-ray beam is only a few micrometers. The penetration depth of the X-ray beam was evaluated according to [20]. It can be argued that 70 % of total diffraction intensity was obtained from a depth of about 1 μm calculated for a scattering angle of 27° (the middle of the analyzed spectrum) and a linear absorption coefficient of 594 cm^{-1} [33]. The experiment was conducted at the Microfocus Beamline ID13 of the European Synchrotron Radiation Facility.

ASS AISI 321 was used as the experimental material in this study. The elemental composition of the alloy is presented in Table 1. The sample was prepared from a round bar by lathing. As shown in Fig. 1b, the initial width of the sample's work surface is 1.2 mm. The work surface was prepared carefully by grinding and polishing to a

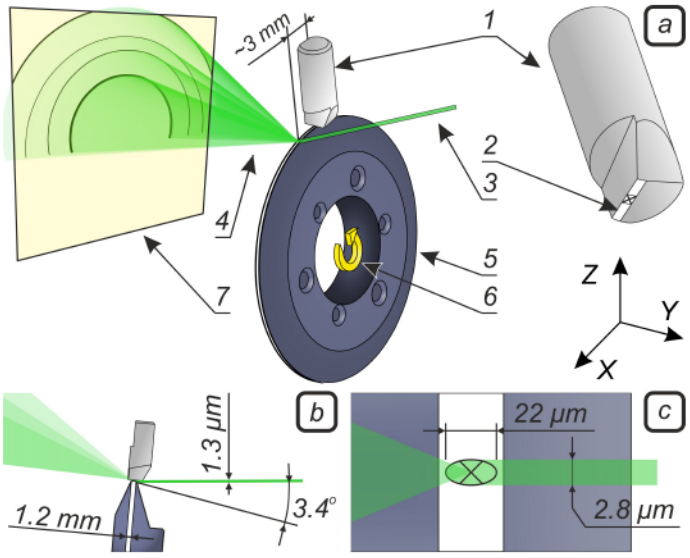


Figure 1: (a) The scheme of the experiment on dry friction with simultaneous diffraction analysis: 1 – the pin; 2 – the work surface of the pin is highlighted with a white rectangle. The apparent contact area is marked with a crossed rectangle; 3, 4 – the incident and diffracted radiation, respectively; 5 – the sample; 6 – the rotation direction; 7 – the two-dimensional detector Dectris EigerX 4M; (b) the scheme of grazing incidence geometry; (c) the footprint of the beam on the work surface (not to scale).

mirror finish using diamond pastes. The final stage of sample preparation was austenitization at 1000 °C for 1 hour and subsequent oil quenching. The heat treatment was carried out in a vacuum. As a result of recrystallization, it can be assumed that all residual stresses in the surface layer of the sample were caused only by quenching rather than by the prior mechanical treatment.

Table 1: Elemental composition of AISI 321

C	Cr	Ni	Ti	Mn	Si	N	Mo	S	P	Fe
0.07	17.17	8.55	0.33	0.40	0.58	0.06	0.05	0.002	0.018	balance

The cemented carbide (WC-20Co) pin was prepared by wire electrical discharge machining. The material of the pin was chosen because of its high hardness and wear resistance. The frictional interaction occurs between the lateral surface of the steel sample and the work face of the pin, as shown in Fig. 1a. As the pin's working area interacts with the sample's cylindrical surface, the actual contact area is difficult to estimate. From a purely geometrical consideration, the apparent contact area is estimated to be approximately 1.2 mm^2. However, in cases with high plastic deformations, the contact area can be significantly larger.

2.2. Raster scanning (mapping) of the friction surface

The deformation of the surface region caused by friction can be nonuniformly distributed over the surface of the sample. Raster scanning over the friction surface using a synchrotron X-ray beam was implemented to analyze the spatial variation of the material's structure. For this purpose, the experiment was interrupted after a certain number of sample revolutions, and the friction surface was then mapped according to the scheme shown in Fig. 2. During scanning, the friction device, pin, and sample were moved along the Z- and X-axes in increments of 1.3 and 5 μm, respectively. The footprint of the X-ray beam on the friction surface was 22 × 2.8 $μm^2$. The result of scanning was an M × N array consisting of 121 (along the Z-axis) × 410 (along the X-axis) = 49610 diffraction patterns. The raster scanning results presented in the paper were not averaged. Each pixel in maps represents the information from the corresponding point on the sample's surface. Data on the intensity and FWHM of the diffraction peaks were extracted from the obtained patterns. These data were used to generate maps with a resolution of 121 × 410 pixels, illustrating the distribution of the intensity and FWHM of peaks over the friction surface.

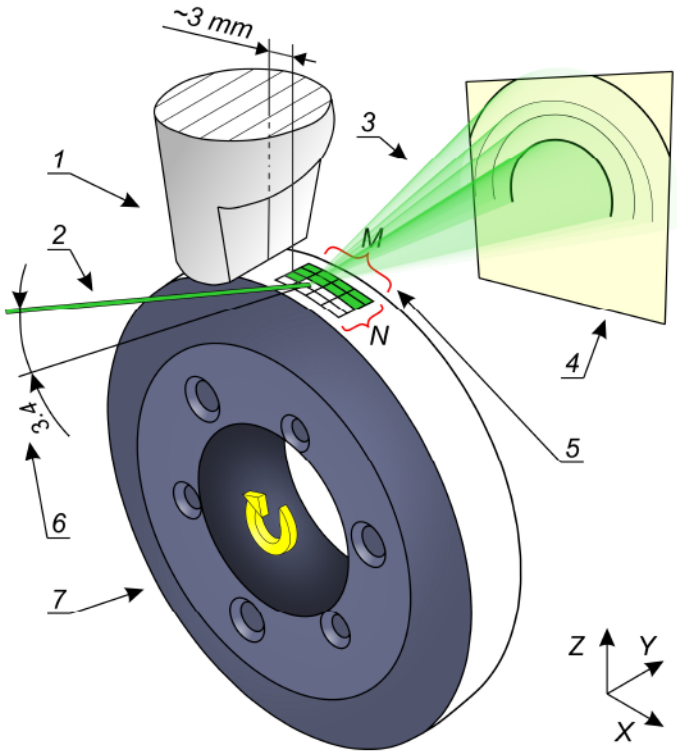


Figure 2: The scheme of surface scanning (not to scale): 1 – the pin; 2 – the incident beam; 3 – the scattered radiation; 4 – the two-dimensional detector; 5 – the scanned area consisting of M × N points, where M and N are equal to 410 and 121 respectively; 6 – the grazing angle; 7 – the sample.

2.3. Ex situ observation of materials

On completing the friction test, the sample was cut carefully by wire electrical discharge machining. The microstructures of the pin and the disk surfaces were studied by light mictoscopy and SEM using a Carl Zeiss Axio Observer A1m and a Carl Zeiss EVO 50 coupled with an energy-dispersive spectrometer (EDX) Oxford Instruments X-Act, respectively. Different cross sections of the disk were prepared by grinding and polishing with abrasive paper and diamond suspensions. The structure of the specimens was revealed by etching with aqua regia solution (HNO_3 + 3HCl). The hardness and Young's modulus were measured using the nanohardness tester Nanoskan-3D (FSBI TISNCM) equipped with the Berkovich indenter. The procedure of hardness measurement and scheme of nanoindentation (Fig. S1) are described in detail in Supplementary material 3.

3. Results

3.1. Results of raster scanning over friction surface

The results of intermediate raster scanning over the sample's surface are shown in Fig. 3, which represents the distribution of intensities of (111) reflection of austenite (Fig. 3a-g) and (110) reflection of α'-martensite (Fig. 3h-n). In the initial state (i.e., for the as-quenched sample), the intensity of (110) reflection of the α' phase is close to zero for all points over the friction surface (Fig. 3h). The absence of such reflection means that the material consists mainly of austenite after vacuum quenching (Fig. 3a). Other phases, such as oxides and carbides, are also observed on the surface. The information about them can be found in Supplementary Material 4.

There is no noticeable change in the phase constitution at the friction surface after two and five cycles of sliding (Fig. 3b, i and Fig. 3c, j). After 30 cycles, a narrow wear track forms on the sample's surface, seen clearly as a bright parabolic line in Fig. 3k or as a corresponding dark line in Fig. 3d. The intensity of austenite peaks in this

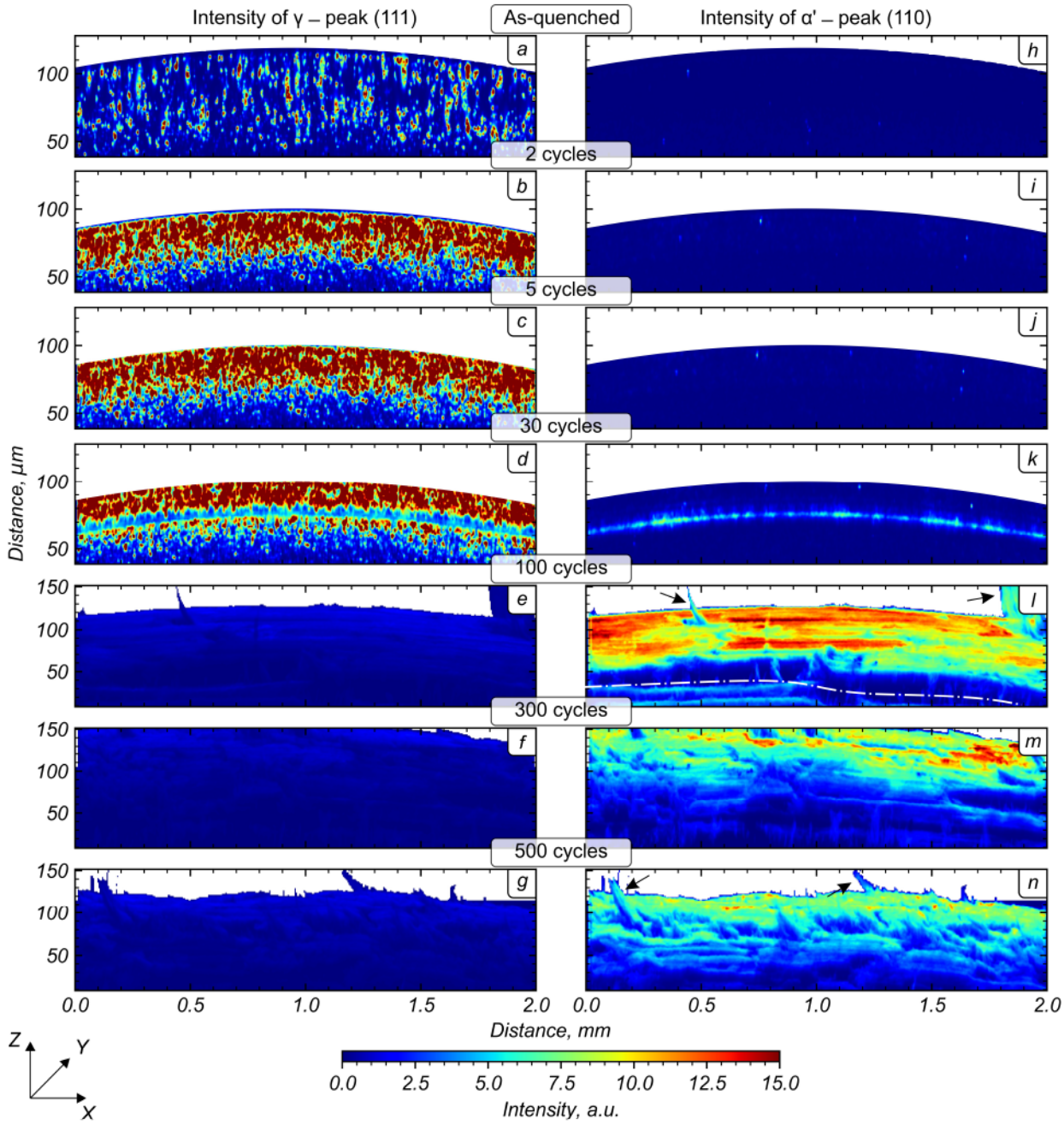


Figure 3: Distribution of the diffraction maxima intensity over the friction surface at different stages of friction: (a-g) (111) reflection of the γ phase; (h-n) (110) reflection of the α′ phase. The white dashed-dotted line shows the microcrack profile, and the arrows show the separating wear debris.

region decreases, whereas the intensity of α′-martensite reflections increases. This effect indicates the occurrence of friction-induced martensite transformation.

Considering the phase constitution along the newly formed wear track (Fig. 3k), as well as at distances of 150 μm and 300 μm from it, we found that the α′-martensite peaks become less distinguishable as the distance from the wear track increases. It means that the most significant structural transformations are concentrated in this narrow groove during the first few dozen friction cycles. This is also confirmed by peaks broadening (indicating the accumulation

of crystal lattice defects) of austenite. The highest value of the FWHM (0.25°) of austenite is observed in the wear track region where martensitic transformation is observed. The average FWHM value decreases to 0.13° and 0.09° at distances of 150 μm and 300 μm respectively. One can refer to Supplementary material 4 for additional information.

The question of whether it is possible to generate the ε-martensite in the ASS because of friction is of particular interest. The formation of the ε phase was not reported in many previous studies devoted to structural transformations in ASSs during mechanical treatment [34, 35, 36], including those that studied the friction of these alloys [10, 37]. Apparently, this is because the state of the material in the mentioned works was studied post-mortem (i.e., at the end of the test), when all the intermediate stages of martensite transformation had already occurred. For this reason, the formation of the ε phase was not revealed by Makarov et al. even using transmission electron microscopy [10]. In this study, we could detect weak though distinct reflections of ε-martensite (Fig. S4b-d presented in Supllementary materials 3) because of the use of a bright X-ray source and thorough analyses of the initial stages of friction.

According to Fig. 4, the highest intensity of (101) reflection of the ε phase is observed in the area between curves 1 and 2, that is, at some distance from the wear track. It is known that γ-ε transformation in ASSs occurs at relatively small strains. According to Padilha and Rios, the maximum volume fraction of the ε phase in the AISI 304 steel is observed when the strain value is 5 % [38]. A subsequent increase in strain causes ε-α′ transformation. Apparently, a similar situation is observed in this case. For instance, after the first few dozen revolutions, the highest strain is common for the newly formed wear track area (close to curve 1) and, in this region, the material probably undergoes γ-ε-α′ transformation (although the possibility of direct γ-α′ transformation in this region cannot be completely excluded). The ε phase is located primarily at some distance from the wear track, that is, in the area with lower strain values. Between 30 and 100 cycles, α′-martensite becomes the predominant phase over the whole friction surface.

After 100 friction cycles, the ε phase is not revealed by raster scanning. Based on Fig. 3l-n, which correspond to 100, 300, and 500 cycles of friction, respectively, the sample's surface gradually acquires a complex topography with multiple microcracks and debris particles on it.

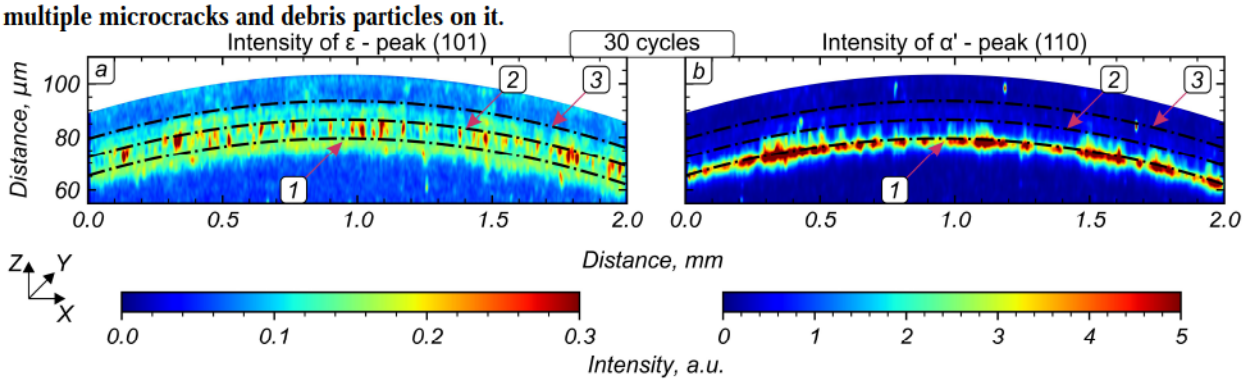


Figure 4: Distribution of intensity of (101) ε (a) and (110) α′ (b) diffraction maxima after 30 cycles of friction loading.

One manifestation of severe wear is a partial fracture of the cemented carbide pin, which was revealed using raster scanning (Fig. 5). The diffraction patterns of an area of the sample containing WC particles are specified by arrows 1-6 in Fig. 5b. The corresponding XRD patterns confirming the presence of the WC phase (P-6m2) are shown in Fig. 5e. From the data presented in Fig. 5a, b, one can conclude that the partial fracture of the pin occurs between 30 and 100 friction cycles. After the partial fracture of the pin's contact surface, its particles may take part in the friction process, particularly in the formation of the MML. It was observed that the amount of WC on the sample's surface decreases in the process of further frictional interaction. This decreasing amount is probably due to the WC particles being removed gradually from the interface by squeezing them out to the sides or separating them from the surface and the steel particles (Fig. 5c, d). The phenomenon of pin fracture was not observed during the rest of the experiment.

One can infer from this subsection analysis that sliding friction of the AISI 321 sample with the cemented carbide pin is accompanied by a complicated set of phenomena, the most interesting of which is martensitic transformation. It has the greatest effect on the process, leading to significant hardening of the surface layer and, as a result, to wear of the cemented carbide pin. The dynamics of microstructural parameters during the friction test are considered in the

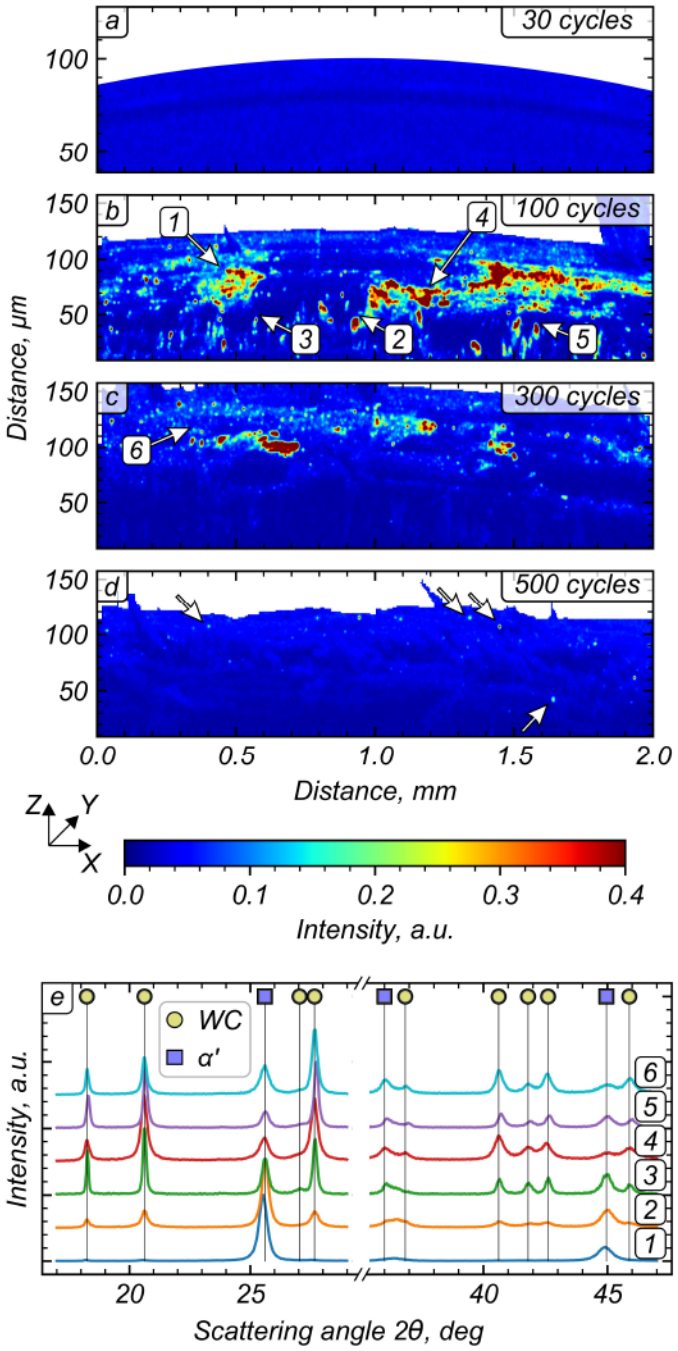


Figure 5: (a), (b), (c), and (d) Distribution of intensity of the (111) peak of WC after 30, 100, 300, and 500 friction cycles, respectively; (e) diffraction patterns corresponding to arrows #1-6.

following section devoted to operando investigations.

3.2. Operando analysis of phase transformations under dry sliding

In the initial (as-quenched) state, the surface layer of the sample consists mainly of austenite, a small amount of α′ and ε phases, and iron oxide. On completing the friction test the surface consists mainly of friction-induced

α′-martensite. The diffraction patterns of the sample in the initial state and after the friction test are presented in Supplementary Material 5 (Fig. S6).

One can trace the evolution of phase constitution during the friction process using the color map shown in Fig. 6. This diagram is a time-ordered sequence of diffraction patterns, each of which characterizes a specific friction cycle. The procedure used to plot this diagram is described in detail in Supplementary Material 5 (Fig. S8). From Fig. 6a-c, it follows that during the first dozen friction cycles, the γ phase is transformed into α′-martensite, which occurs via the intermediate formation of ε-martensite (Fig. 6c). For this reason, the initial stage of friction is of particular interest and requires detailed consideration.

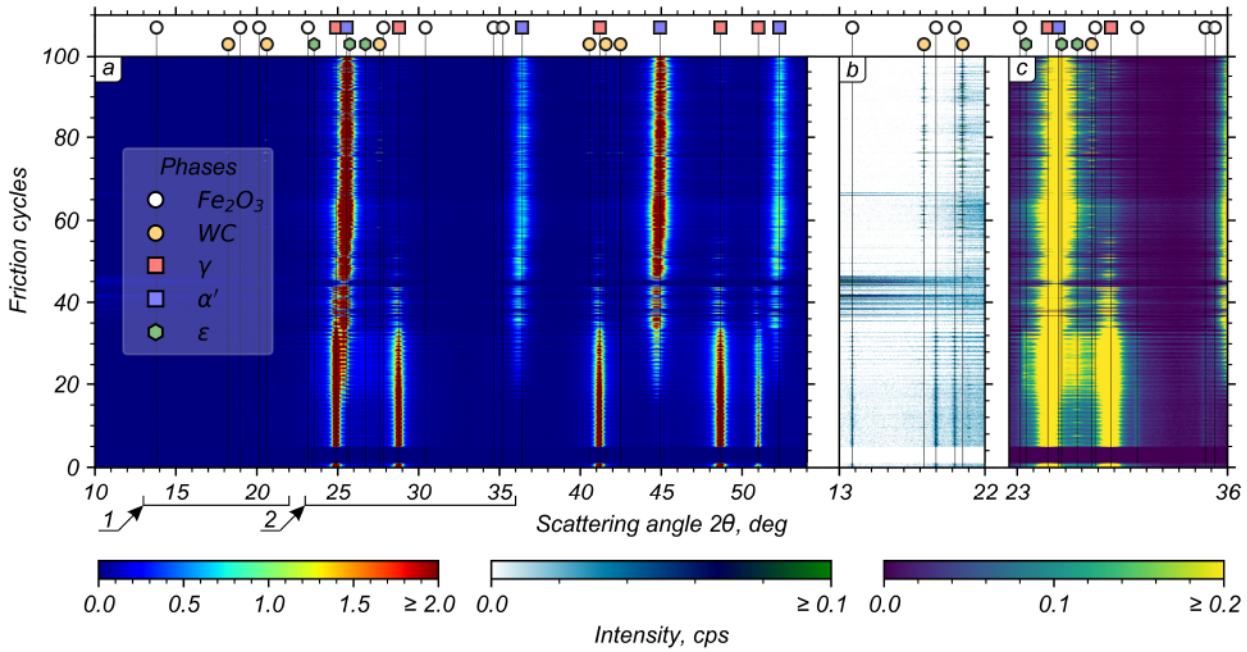


Figure 6: (a) The map representing the change in the phase constitution of the surface layer from the initial state up to 100 cycles of friction: arrows 1 and 2 indicate areas of the map shown in a different intensity scale in (b) and (c), respectively.

The friction-induced transformations can be examined in detail by analyzing the variation of the integral intensity of the γ, α′, and ε phases maxima. From Fig. 7a, b, it follows that the mechanically induced martensitic transformation begins after 16 cycles of interaction between the sample and the pin, which is manifested in a rapid increase in intensities of the α′ and ε reflections. Operando studies clearly show the formation of ε-martensite in the initial stage of friction. The intensity of its diffraction maxima increases gradually between 16 and 23 friction cycles, after which it remains little changed until 32 cycles and reduces sharply to 35 cycles. The weak reflections of ε-martensite are still observed up to about 45 cycles (Fig. 6c). As illustrated in Fig. 7c, 35 cycles after the test beginning, the fraction of the α′ phase at the sample's surface exceeds 50 %. After 50 revolutions, the structure is almost entirely represented by α′-martensite. The evolution of the phase constitution throughout the test is presented in Supplementary Material 5 (Fig. S9).

When considering the operando results, one has to take into account the penetration depth of X-ray beam, which is equivalent to ca. 1 μm. It means that both martensite phases can be detected only in a layer of ca. 1 μm thick. According to Fig. 7 α′- and ε-phases were gradually generated up to 35th cycle, however, further frictional interaction led to decrease in integral intensity of the latter. We believe that this effect is associated with the gradual ε-α′ transformation in a studied layer. We also believe formation of ε-phase is still possible in material that is deeper than irradiated layer though we were not able to detect it.

The shift of γ peaks during the test indicates that austenite decomposition is accompanied by an increase in the probability of deformation stacking fault (DSF) formation. One can estimate probability density of DSF formation (α_{SF}) in FCC-structures using formula 5 presented in Supplementary material 5. Its derivation can be found in [39].

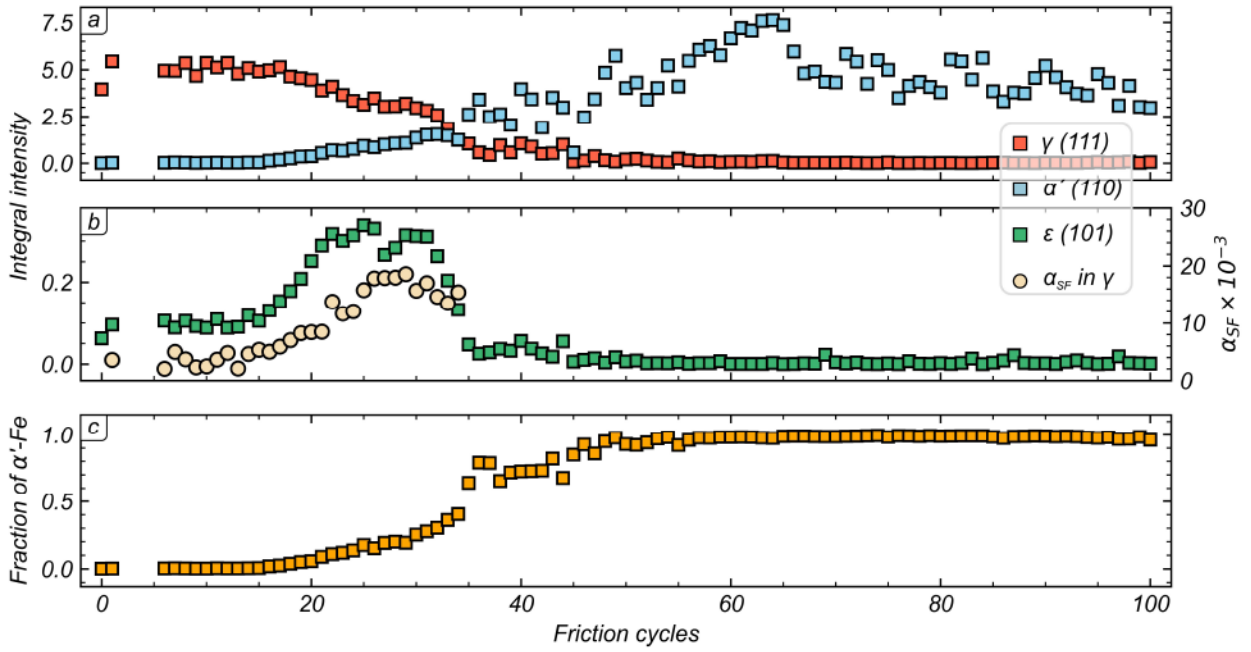


Figure 7: The integral intensity of the γ and α′ (a) and ε phases (b) diffraction maxima depending on the number of friction cycles. The plot (b) also illustrates the stacking fault probability in austenite. (c) The fraction of the α′-martensite during the test.

The calculated α_{SF} is shown in Fig. 7b. It means that during friction, the atomic planes stack in a sequence typical of hexagonal-close packed (hcp) lattice form in austenite [39]. These local faults can be considered as ε-martensite crystallites. The more crystallites that are formed, the greater the number of planes that satisfy Bragg's condition; therefore, the intensity of ε-martensite peaks will be higher. From Fig. 7b, one can observe that the intensity of the ε-martensite peaks and α_{SF} are correlated.

3.3. Peaks' profile change caused by friction

As α′-martensite is the predominant phase during most of the test, we divided the friction process into the run-in stage (ca. 100 cycles) and the steady-state stage by analyzing the alteration of FWHM. The variation of FWHM of both α′ and γ phases diffraction maxima during the friction test is shown in Supplementary Material 6 (Fig. S10).

3.3.1. Analysis of the first 100 friction cycles

The friction-induced broadening of the (111) γ and (110) α′ peaks is shown in Fig. 8. Based on the FWHM dynamics, a few specific stages were identified, marked with numbers, and bounded by vertical lines in Fig. 8. The first stage (up to 15 friction cycles) was characterized by a slight change in the FWHM of the austenite's diffraction maxima, which indicates that, at this stage, the sample deforms predominantly elastically. However, the raster scanning results shown in Fig. 3 reveal that the refinement of austenite is observed already after two friction cycles, indicating the occurrence of plastic deformation of the subsurface layer. It is probably impossible to observe the peaks' broadening during the first friction cycles as the thickness of the deformed layer at this stage is significantly less than the X-ray penetration depth, that is, the main part of the radiation was scattered by the original (undeformed) austenitic structure.

At the next stage (from 15 to 55 friction cycles), the (111) γ maximum broadens from 0.11 to 0.31 2θ degrees. At the same time, the (110) α′ peak appears in the diffraction patterns. From the very beginning, it has a relatively high FWHM value. During the subsequent seven revolutions (from 55 to 62), the FWHM of (110) α′ reaches the maximum value of approximately 0.42 2θ degrees. Then, after 62 friction cycles, it decreases slightly and reaches a threshold value. One possible explanation for this behavior of the FWHM of the (110) α′ peak in the range from 55 to 69 cycles is associated with a partial fracture of the cemented carbide pin, which could probably occur after the 55th cycle (Fig.

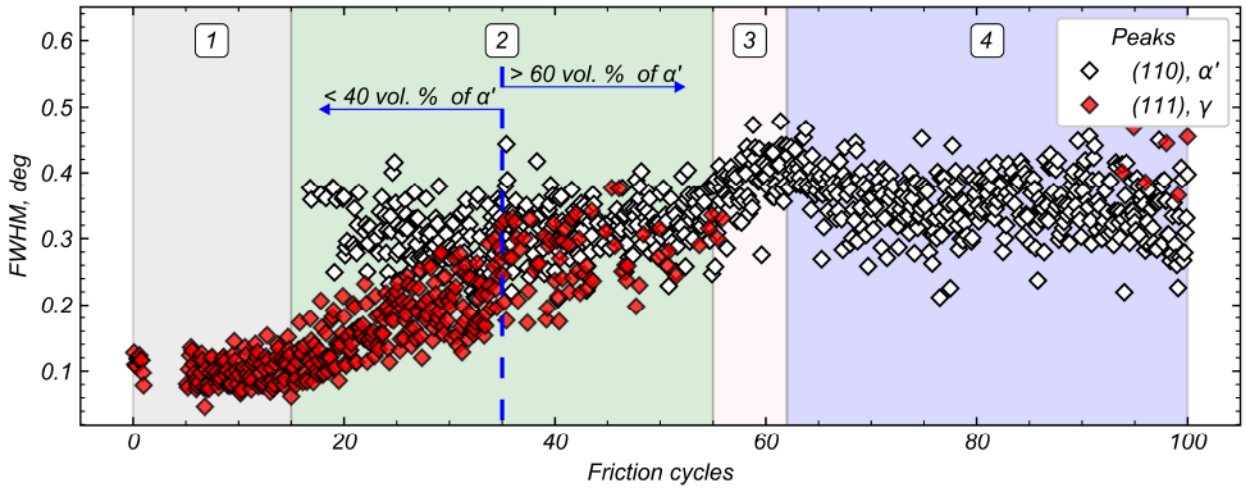


Figure 8: The effect of friction on the FWHM of the (111) and (110) peaks of austenite and martensite, respectively. The dashed line shows the moment when the volume fraction of α′-martensite sharply increased (see Fig. 7c.).

6). As a result, the most deformed layer could be cut from the surface because of the formation of a sharp edge on the pin's working surface. Another reason explaining this phenomenon could be the first seizure between the sample and the pin, which occurred when the oxide film on the sample's surface was fully broken. Both processes are confirmed by the post-mortem SEM analysis (Fig. S11) of the pin (see Supplementary material 7 for details). Another interesting observation is the appearance of austenite in the range from 90 to 100 cycles. We believe that this phenomenon is due to the destruction of the MML, which exposes the underlying austenite.

Based on Fig. 8, it can be concluded that steady-state friction is achieved after ca. 69 cycles of friction. No significant changes in the peaks' FWHM were observed after that. This means that the threshold value of defect concentration is achieved at the sample's surface.

3.3.2. Friction-induced structural evolution

Fig. 9 illustrates the variations in the structural parameters (CSR size (D), dislocation density (ρ), dislocation outer cut-off radius (R_e), and Wilkens parameter(M)) with the number of friction cycles. The vertical regions in Fig. 9 correspond to those marked in Fig. 8. The calculation procedure is briefly described in Supplementary material 8.

There are no significant changes in the CSR size of the γ phase during the first friction cycles. Their average value is about 30 nm (Fig. 9a). After 35 friction cycles, the CSR size reduces by half. The threshold value is reached at this stage and maintained until approximately 55 friction cycles, that is, until the austenite is wholly transformed to martensite at the friction interface. CSR sizes of α′-martensite do not alter materially from its formation moment at the beginning of the steady-state stage until the end of the test. Their value is equal to approximately 15 nm, except for the interval from 55 to 67 cycles of friction loading. The CSR sizes decrease for a short time to approximately 12 nm and then return to the threshold value of 15 nm.

According to Fig. 9b, at the beginning of the experiment, the dislocation density of the γ phase is low (approximately 10^{12} cm^{-2}). This value virtually does not change during the first 15 cycles. The Wilkens parameter of the γ phase at the beginning of the experiment is also low (approximately 0.3, Fig. 9d), indicating that dislocations form some ordered arrangement, such as dislocation walls. The dislocation density in austenite increases starting from the 15th cycle and doubles 23 cycles later from the beginning of the test. Up to the 35th cycle, the dislocation density changes insignificantly. However, after the 35th friction cycle, the dislocation density of the γ phase increases sharply to about 4×10^{12} cm^{-2}. At the same time, the integral intensity of the ε-martensite peaks approaches zero, as shown in Fig. 7b. Significant fluctuations in the dislocation density in austenite are observed on further frictional loading. It decreases to 3.2×10^{12} cm^{-2} and then increases with significant oscillations, reaching 5.6×10^{12} cm^{-2} in the range from 40 to 55 cycles. The Wilkens parameter of this phase increases gradually and eventually doubles from the beginning of the experiment until complete austenite decomposition. An increase in the Wilkens parameter indicates that the

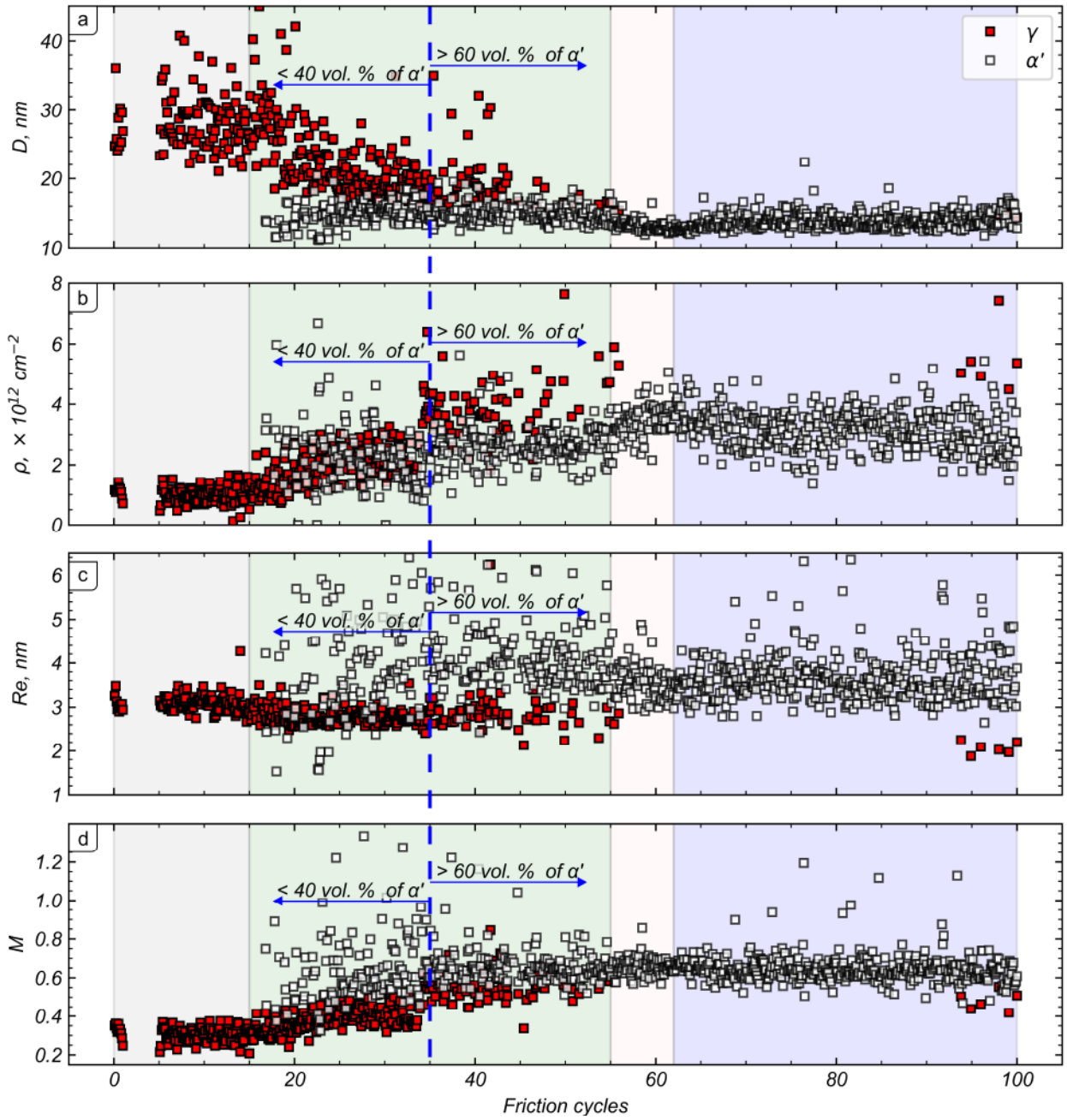


Figure 9: Changes in the size of the CSR (a), the dislocation density (b), the dislocation outer cut-off radius (c), and Wilkens parameter (d) during friction. The dashed line shows the moment when the volume fraction of α′-martensite sharply increased (see Fig. 7c.).

dislocation structure of austenite becomes less ordered gradually. However, the chaotic arrangement of dislocations (which corresponds to $M \gg 1$) is not achieved. As for the dislocation outer cut-off radius, no significant changes in this parameter are observed, except for a slight decrease in region 2 (from 15 up to 55 friction cycles) of Fig. 9c at the very beginning of the martensitic transformation.

A few words should be noted here regarding the stress screening. Stress fields around the dislocations depend not only on their density, but also on their mutual arrangement. If the stress fields around individual dislocations screen

each other, the total distortion of the crystal lattice is reduced compared to an unscreened disordered arrangement of dislocations. This effect is expressed as a decrease in the outer cut-off radius. The change in the R_e of austenite confirms the probability of stress field screening during the interaction of dislocations.

The α′-martensite dislocation density is sufficiently high from the moment of its formation up to the 34th cycle (from 2.3 to 3.5 × 10^{12} cm^{-2}). It reduces to 1.5 × 10^{12} cm^{-2} by the 35th test cycle and subsequently increases and reaches the threshold value of 2.5 × 10^{12} cm^{-2}. The maximum dislocation density, just as in the CSR sizes, is observed after 62 friction cycles (ca. 3.8 × 10^{12} cm^{-2}). The Wilkens parameter and dislocation outer cut-off radius of α′-martensite vary only slightly throughout the experiment.

It would be interesting to estimate the amount of energy expended on certain structural transformations in the process of friction. Given the coefficient of friction presented in Table S1 (Supplementary material 2), the work done by friction can be calculated as $A = \mu F S$ (J), where μ is a friction coefficient; F is a normal force on the sliding interface, N; $S = 2\pi Rn$ is a friction path, m; R is a radius of disk, m; n is a number of friction cycles. Thus, the energy consumed on friction is approximately 25 J/cycle. It means that ca. 375 J was consumed before the 15th cycle, when the martensite transformation was observed. It also means that ca. 875 J was consumed when the maximum fraction of ε-martensite was reached in a layer of 1 μm thickness after the 35th cycle. Further interaction leads to the disappearance of diffraction maxima of ε-martensite. Approximately 1125 J were consumed after the 45th cycle when a layer of 1 μm thickness composed mainly of friction-induced α′-martensite. Finally, the steady-state wear mode is established after 69 friction cycles that correspond to 1725 J. Here, however, it should be noted that most of this energy is spent on elastic deformation and heating of the sample, and only a small fraction is spent on phase transformations themselves [15, 40, 41, 42] .

3.4. Metallographic analysis

3.4.1. Observation of structure on completion of the friction test

The metallographic analysis of the sample on completion of the sliding (500 cycles later from the test beginning) is shown in Fig. 10. The original cross section of the sample indicated by the dashed line changes in shape because of high plastic deformation coupled with wear (Fig. 10a), leading to the formation of burrs. One can identify several layers in the sample's cross section:

1. the MML that consists mainly of the material of the sample's surface and has a pronounced boundary with the underlying layers of the sample (Fig. 10b, c);
2. deformed layer below the MML (Fig. 10c);
3. undeformed base metal.

According to the data presented in Sections 3.1 and 3.2, the MML consists mainly of α′-martensite. Cyclic friction loading of the MML results in the formation of fatigue cracks. Consequently, it is possible to observe the delamination of the material (Fig. 10b, c) and/or the local fracture of the layer (Fig. 10d). An interesting effect caused by friction is the fragmentation of titanium carbides. Its particles are elongated in the sliding direction. An example is shown in Fig. 10d.

3.4.2. Examination of the sample's surface on completion of the test

Considering the severe experimental conditions, we expected to observe the working surface to exhibit a rough structure. According to Fig. 11a, the friction surface of the steel sample is characterized by large areas exposed to plastic flow. In some areas, the width of the worn surface reaches 1.6 mm. The phenomenon observed is probably the result of the high ductility of the alloys in which martensitic transformation occurs. A similar behavior was discussed previously in [43, 44].

Nevertheless, most of the sample surface possesses a different structure, as demonstrated in Fig. 11b, c. This structure is a product of two factors: adhesion and material delamination. In addition, the work face of the sample contains multiple grooves parallel to the rotation direction and wave-like structures. The latter (indicated by the white arrows in Fig. 11b, d) indicates a layering of the material. Layered material can contribute to the formation of the MML and the vortex-like structures. The latter ones shown in Fig. S12 presented in Supplementary material 7. The cracks were detected because of layering, as shown in Fig. 11d by arrows 1 and 2. Apparently, the combination of critical stresses and accumulated local deformations can result in material fragments being sheared off, inducing a

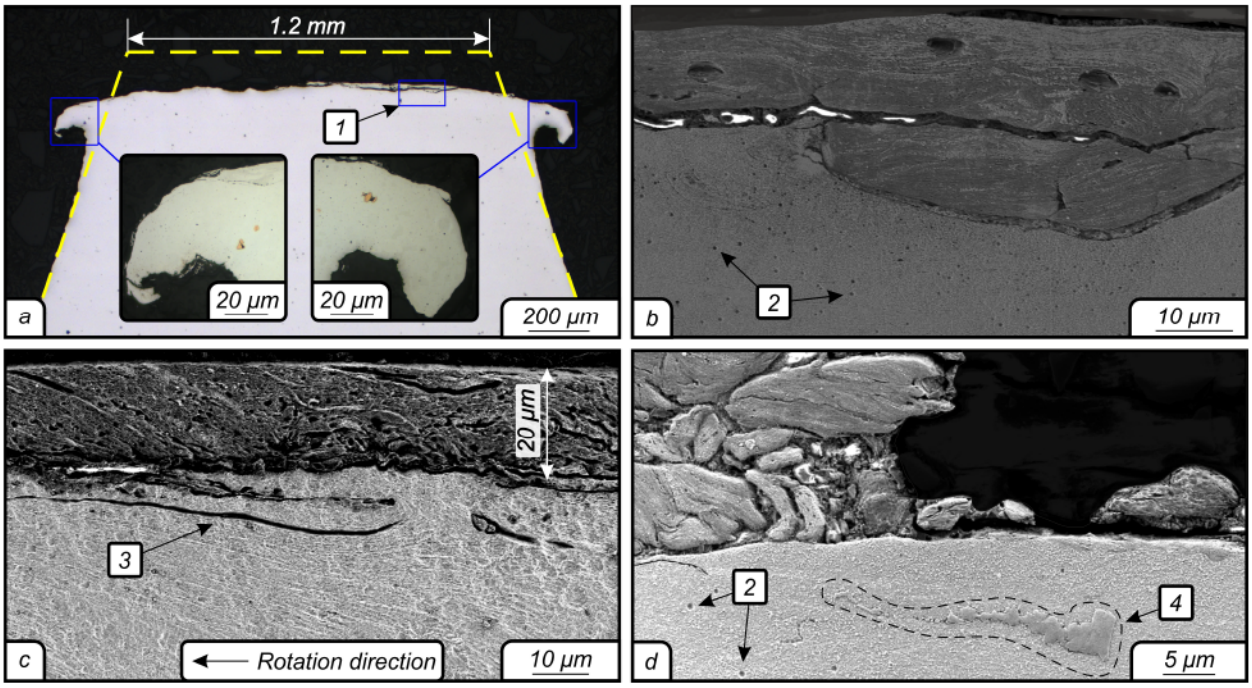


Figure 10: (a,b) The YZ section of the sample at the end of the test (dashed line indicates the initial shape); (c) the MML structure in the XZ section; (d) delamination of the MML. 1 – The area represented in image (b); 2 – dislocation pits; 3 – delamination cracks; 4 – a fragmented particle of TiC. The arrangement of the X-, Y-, and Z-axes are shown in Fig. 2.

delamination process through the interface of the MML and then forming the wave-like structures, as shown by the arrows in Fig. 11d. Fig. 11e shows the surface area where the wear debris is separated. We believe that this kind of surface fracture is due to the combination of delamination processes and spalling. As a result, the surface appears like it is shown in Fig. 11c, f. From Fig. 11f, it is also clear that the fractured area is characterized by a layered structure (the arrows indicate several pronounced layers).

3.4.3. Nanoindentation results

In Fig. 12, the nanohardness and the Young's modulus of the work surface after 500 friction cycles are shown as derived from nanoindentation measurements. The average hardness of the MML reaches up to 8 GPa. A sharp decrease in hardness is observed at a distance of 20 μm from the surface. This decrease can be attributed to delamination cracks formed between the MML and the underlying material. At a distance between 25 and 50 μm from the surface, the hardness decreases gradually to about 4 GPa. The Young's modulus of the MML shows some fluctuations, indicating a different resistance of the MML structure to external mechanical action. The fluctuations go down to about 30 μm below the surface; after this, it seems to be quite constant. A similar behavior was observed by Tarasov et al. [45].

4. Discussion

4.1. Formation of ε-martensite

This experiment shows that friction-induced martensitic transformation in AISI 321 steel occurs with the intermediate formation of the ε phase. Based on the operando analysis (Fig. 6 and Fig. 7b), it can be concluded that the ε phase appears only during a short period of the experiment . The formation of ε-martensite begins after 15 friction cycles. This is preceded by a gradual accumulation of strain in austenite. When a threshold value of strain is achieved, the martensitic transformation can occur. Further frictional interaction leads to the formation of fresh microvolumes of ε-martensite thereby leading to an increase in the integral intensity of the corresponding diffraction maxima. The

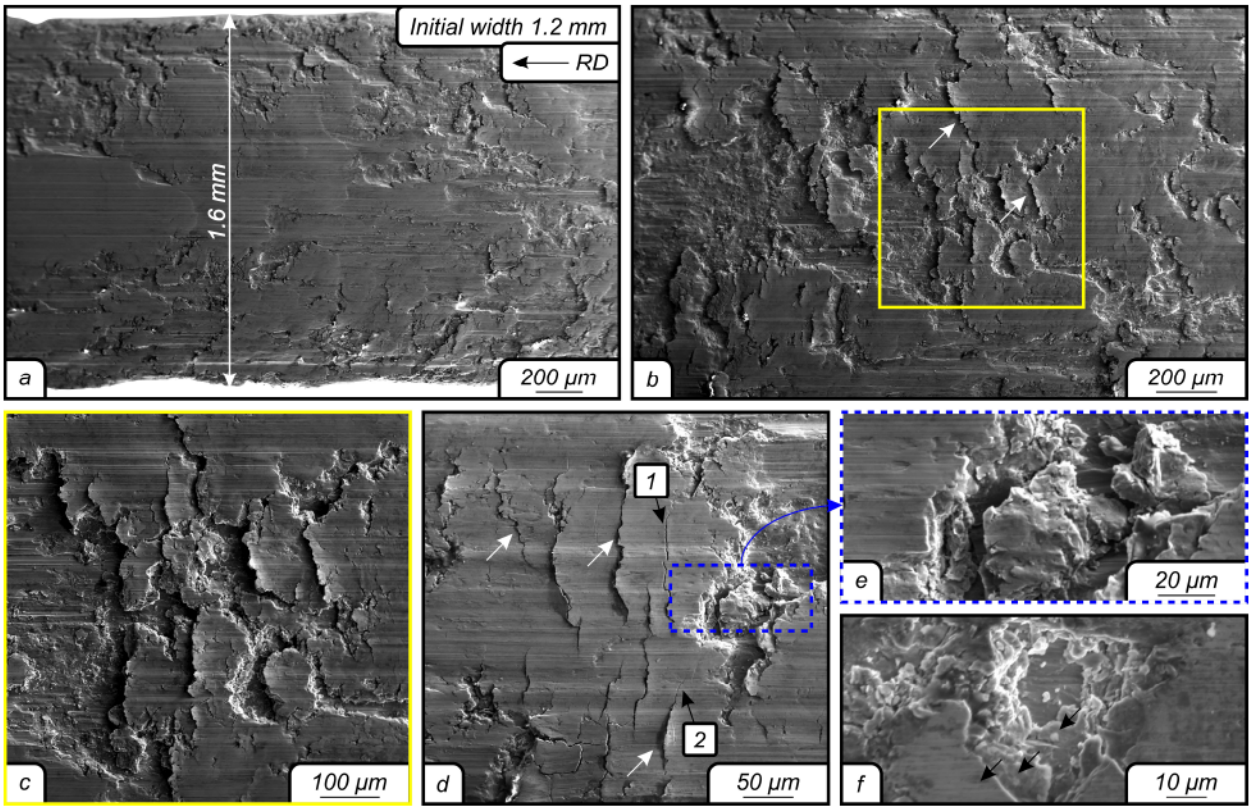


Figure 11: (a, b) The structure of the work face of the steel sample on completion of the experiment; (c) the area marked with a rectangle on image (b); (d) the layered structure; (e) the area restricted by the dashed rectangle on image (d); (f) the layered structure in the spalling area. 1, 2 – Cracks between layers.

value of accumulated strain exceeds the threshold required for the ε-α′ transformation by the 35th cycle. At this point, the material almost completely transforms into the α′ phase. The probability of DSF generation has a similar trend (Fig. 7b). The absence of the ε phase in the surface after the 35th cycle does not mean that it does not form during friction. As it was concluded from analysis of Fig. 4a, the ε phase forms at relatively small strains and decomposes when the strain increases. Considering the penetration depth of the incident X-ray (a few micrometers) and with respect to the thickness of the severely deformed MML (ca. 20 μm), it is clear that XRD could not detect the formation of the ε phase below the MML. The deformation below the MML can be seen clearly in Fig. 10c and Fig. S12 (see Supplementary material 7), which show that grains (or subgrains) align along the sliding direction. The deformation in this layer can also be tracked by observations of TiC fragmentation (Fig. 10d). As the deformation below the MML decreases gradually, one may always find such a layer that is deformed exactly as required for γ-ε transformation.

4.2. Stages of structural evolution

As illustrated in Fig. 8, four stages of frictional interaction were identified based on operando and ex situ investigations. There were no significant changes in the sample's microstructure during the first stage (up to 15 friction cycles). This is because of the small thickness of the deformed layer at this stage, which was probably considerably smaller than the penetration depth of X-rays used in this experiment.

The frictional effect becomes more pronounced at the second stage (from 15 to 55 cycles of friction, as shown in Fig. 9). The dislocation density change in austenite is of particular interest. One can observe its slight increase after 23 friction cycles. After that, the dislocation density of austenite reaches a value that changes little up to 34 cycles. Apparently, the plateau observed is associated with relaxation processes occurring in austenite and is caused by the following reasons:

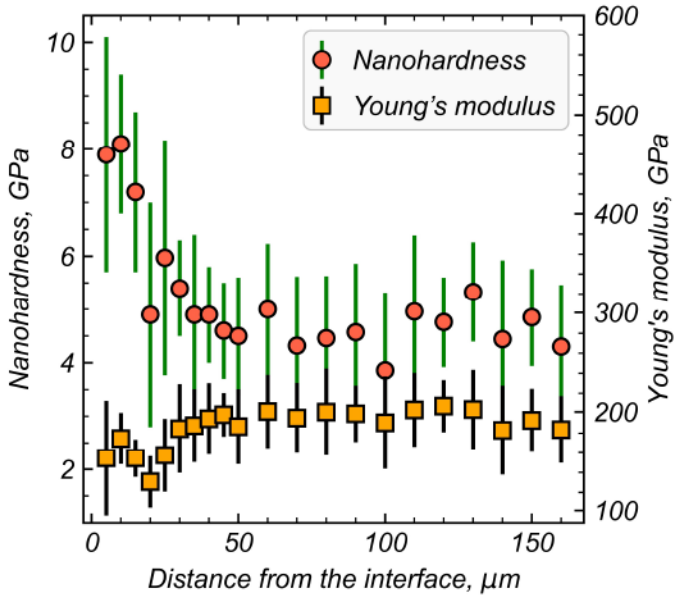


Figure 12: Nanohardness and Young's modulus of the sample after 500 friction cycles.

1. **Once a certain threshold concentration of defects in the austenite is reached, martensitic transformation could occur. In this case, the martensite inherits the defects of austenite, and the dislocation density in the remaining austenite does not exceed the threshold value. This is confirmed by the calculation of the dislocation density of the α′ phase. Fig. 9b shows that dislocation densities in both α′ and γ phases have similar values. A similar effect was previously observed during the abrasive wear of annealed AISI 1044 steel, which was accompanied by reaustenitization, followed by martensitic transformation [2] and during the deformation and partitioning of medium manganese steel [44]. In both cases, α′-martensite inherited a high dislocation density from metastable austenite.**
2. **When martensite forms in austenite because of mechanical action, the elastic strains accumulate at the interphase boundary. Such accumulation can lead to a violation of phase coherence [46]. In this case, misfit dislocations are formed at the interface, which provides stress relaxation between the mating phases. Meanwhile, there is no increase in the dislocation density (Fig. 9b). This seems to be associated with the formation of a shielded system when the stresses compensate each other. The stress fields around the dislocations should decrease in such a case. This is evidenced by a decrease in the dislocation outer cut-off radius (Fig. 9c). Another jump in the dislocation density of austenite was observed in the range from 34 to 35 friction cycles. Further, the accumulated elastic strains lead to the accelerated formation of the α′ phase, and its volume fraction increases sharply from 40 % to 63 %, as shown in Fig. 7c.**

From the beginning of deformation-induced transformation, peaks of the α′ phase have a sufficiently high FWHM relative to the peaks of the γ phase (Fig. 8). Considering that the broadening of the peaks is due to crystal lattice defects, it can be concluded that such an effect is attributed mainly to one or a combination of the following factors. First, this is associated with the inheritance of the defective γ phase structure, which by the time of α′ phase formation was already saturated with crystal lattice defects. Second, the broadening of the peaks can be related to the small crystallite size of mechanically induced martensite. From Fig. 9a, it follows that the CSR size of α′-martensite is about 12 nm at the beginning of its formation and this value virtually remains the same during this test. The newly formed martensite crystals will obviously prevent the free glide of dislocations in austenite. From this point of view, the ε and α′ phases can be considered as obstacles contributing to precipitation hardening. The dislocation has to either circumvent or cut through them to overcome such obstacles. This results in the generation of new dislocations and manifests itself in the broadening of the diffraction maxima. Finally, such behavior of FWHM may be due to the segregation of impurities to dislocations [47]. This effect should actually lead to a decrease in the stress fields

around the dislocations. However, as nickel (γ stabilizer) has the highest mobility, it segregates more likely on plastic deformation. This can result in the desaturation of some local areas with this element. A decrease in the local nickel concentration leads to the reducing stability of austenite and contributes to the formation of martensite, which inherits the defective state of austenite.

A jump in the microstructural parameters was observed at the third stage (from 55 to 62 friction cycles), as illustrated in Fig. 9. It should be noted that this jump coincides with the moment when WC peaks appeared on the friction surface (Fig. 6b). We believe that jump is associated with the cutting processes of the steel sample as a result of a sharp edge formation after the partial fracture of the pin's working surface.

At the next stage (from 62 friction cycles onward), a decrease in the microstructure parameters to the threshold value was detected, which, apparently, is caused by establishing a new contact area between pin and disk, as shown in Fig. S11a . Thus, it can be assumed that after 69 cycles of friction, the contact pair reached the steady-state friction conditions.

5. Conclusions

This paper presented the results of operando and ex situ analysis of the structural evolution of AISI 321 steel under dry sliding friction using synchrotron XRD. The data obtained were analyzed thoroughly and confirmed by the results of the metallographic analysis; they were then compared with the information available in the literature. Based on the research conducted, the following conclusions can be drawn:

1. The decomposition of austenite under friction was observed by synchrotron XRD. As a result of friction, the sample's surface consists mainly of α′-martensite. It appears via the intermediate formation of ε-martensite. The formation of the latter correlates well with the probability of DSF formation in austenite. The γ and ε phases were not observed in the diffraction patterns after 45 friction cycles from the beginning of the test, which is because of the formation of a sufficiently thick MML, consisting mainly of the α′ phase. Meanwhile, the γ-ε transformation continues to occur in the underlying layers.
2. The shape of the γ phase peaks changes significantly during the test. However, the α′-martensite peaks change little throughout the test. This is because the newly forming α′ phase initially contains many crystal lattice defects inherited during the mechanically induced phase transformation.
3. The frictional interaction of AISI 321 steel against the cemented carbide pin is accompanied not only by dislocation and precipitation hardening but also by relaxation processes that consist of the following phenomena: deformation-induced γ-(ε, α′) transformation, dislocation ordering, and formation of shielded dislocation structures. Further interaction of the friction couple leads to a significant increase in wear resistance of the steel surface, which leads to partial spallation of the cemented carbide pin. The peak values of the microstructural parameters reached in the range from 55 to 62 test cycles are apparently associated with the formation of a sharp edge on the pin because of its partial fracture, which leads to the cutting processes. These processes are stopped quickly (by 69 cycles of friction) by establishing a new contact area. After 69 loading cycles, the steady-state wear mode is established.
4. The primary mechanism of wear observed by SEM analysis is the delamination at the interface of the MML with the materials of the underlying deformed layer.

6. Acknowledgments

Research were conducted at core facility of NSTU "Structure, mechanical and physical properties of materials".

7. Funding

This study was funded by the Federal Task of Ministry of Education and Science of the Russian Federation (project FSUN-2020-0014 (2019-0931): "Investigations of Metastable Structures Formed on Material Surfaces and Interfaces under Extreme External Impacts").

References

[1] J. Guimarães, P. Rios, The mechanical-induced martensite transformation in Fe–Ni–C alloys, Acta Materialia 84 (2015) 436–442. doi:10.1016/j.actamat.2014.10.040.
URL https://linkinghub.elsevier.com/retrieve/pii/S1359645414008040

[2] B. Prasad, S. Prasad, Abrasion-induced microstructural changes during low stress abrasion of a plain carbon (0.5% C) steel, Wear 151 (1) (1991) 1–12. doi:10.1016/0043-1648(91)90341-Q.
URL https://linkinghub.elsevier.com/retrieve/pii/004316489190341Q

[3] A. K. Srivastava, K. Das, Microstructural characterization of Hadfield austenitic manganese steel, Journal of Materials Science 43 (16) (2008) 5654–5658. doi:10.1007/s10853-008-2759-y.
URL http://link.springer.com/10.1007/s10853-008-2759-y

[4] D. A. Rigney, Sliding Wear of Metals, Annual Review of Materials Science 18 (1) (1988) 141–163. doi:10.1146/annurev.ms.18.080188.001041.
URL http://www.annualreviews.org/doi/10.1146/annurev.ms.18.080188.001041

[5] K.-L. Hsu, T. Ahn, D. Rigney, Friction, wear and microstructure of unlubricated austenitic stainless steels, Wear 60 (1) (1980) 13–37. doi:10.1016/0043-1648(80)90247-1.
URL https://linkinghub.elsevier.com/retrieve/pii/0043164880902471

[6] A. Smith, The friction and sliding wear of unlubricated 316 stainless steel at room temperature in air, Wear 96 (3) (1984) 301–318. doi:10.1016/0043-1648(84)90043-7.
URL https://linkinghub.elsevier.com/retrieve/pii/0043164884900437

[7] Z. Yang, M. Naylor, D. Rigney, Sliding wear of 304 and 310 stainless steels, Wear 105 (1) (1985) 73–86. doi:10.1016/0043-1648(85)90007-9.
URL https://linkinghub.elsevier.com/retrieve/pii/0043164885900079

[8] A. V. Makarov, P. A. Skorynina, A. S. Yurovskikh, A. L. Osintseva, Effect of the Conditions of the Nanostructuring Frictional Treatment Process on the Structural and Phase States and the Strengthening of Metastable Austenitic Steel, Physics of Metals and Metallography 118 (12) (2017) 1225–1235. doi:10.1134/S0031918X17120092.
URL https://doi.org/10.1134/S0031918X17120092

[9] Y. Sun, Sliding wear behaviour of surface mechanical attrition treated AISI 304 stainless steel, Tribology International 57 (2013) 67–75. doi:10.1016/j.triboint.2012.07.015.
URL https://linkinghub.elsevier.com/retrieve/pii/S0301679X12002538

[10] A. Makarov, P. Skorynina, A. Osintseva, A. Yurovskikh, R. Savrai, Improving the tribological properties of austenitic 12Kh18N10T steel by nanostructuring frictional treatment, Metal Working and Material Science 4 (69) (2015) 80–92. doi:10.17212/1994-6309-2015-4-80-92.
URL http://journals.nstu.ru/obrabotka_metallov/catalogue/contents/viewarticle?id=8284

[11] D. Rigney, L. Chen, M. Naylor, A. Rosenfield, Wear processes in sliding systems, Wear 100 (1-3) (1984) 195–219. doi:10.1016/0043-1648(84)90013-9.
URL https://linkinghub.elsevier.com/retrieve/pii/0043164884900139

[12] V. Panin, A. Kolubaev, S. Tarasov, V. Popov, Subsurface layer formation during sliding friction, Wear 249 (10-11) (2001) 860–867. doi:10.1016/S0043-1648(01)00819-5.
URL https://linkinghub.elsevier.com/retrieve/pii/S0043164801008195

[13] S. Y. Tarasov, Localization of strain in friction, Metal Science and Heat Treatment 48 (5-6) (2006) 226–230. doi:10.1007/s11041-006-0075-1.
URL http://link.springer.com/10.1007/s11041-006-0075-1

[14] L. Chen, D. Rigney, Transfer during unlubricated sliding wear of selected metal systems, Wear 105 (1) (1985) 47–61. doi:10.1016/0043-1648(85)90005-5.
URL https://linkinghub.elsevier.com/retrieve/pii/0043164885900055

[15] D. Rigney, Transfer, mixing and associated chemical and mechanical processes during the sliding of ductile materials, Wear 245 (1-2) (2000) 1–9. doi:10.1016/S0043-1648(00)00460-9.
URL https://linkinghub.elsevier.com/retrieve/pii/S0043164800004609

[16] K. G. Rowe, A. I. Bennett, B. A. Krick, W. Gregory Sawyer, In situ thermal measurements of sliding contacts, Tribology International 62 (2013) 208–214. doi:10.1016/j.triboint.2013.02.028.
URL http://www.sciencedirect.com/science/article/pii/S0301679X13000790

[17] K. Yagi, S. Kajita, T. Izumi, J. Koyamachi, M. Tohyama, K. Saito, J. Sugimura, Simultaneous Synchrotron X-ray Diffraction, Near-Infrared, and Visible In Situ Observation of Scuffing Process of Steel in Sliding Contact, Tribology Letters 61 (2) (2016) 19. doi:10.1007/s11249-015-0636-9.
URL https://doi.org/10.1007/s11249-015-0636-9

[18] M. Miyajima, K. Kitamura, K. Matsumoto, K. Yagi, In Situ Temperature Measurements of Sliding Surface by Raman Spectroscopy, Tribology Letters 68 (4) (2020) 116. doi:10.1007/s11249-020-01356-z.
URL http://link.springer.com/10.1007/s11249-020-01356-z

[19] D. Lychagin, A. Filippov, E. Kolubaev, O. Novitskaia, Y. Chumlyakov, A. Kolubaev, Dry sliding of Hadfield steel single crystal oriented to deformation by slip and twinning: Deformation, wear, and acoustic emission characterization, Tribology International 119 (2018) 1–18. doi:10.1016/j.triboint.2017.10.027.
URL https://linkinghub.elsevier.com/retrieve/pii/S0301679X17304929

[20] S. Kajita, K. Yagi, T. Izumi, J. Koyamachi, M. Tohyama, K. Saito, J. Sugimura, In Situ X-Ray Diffraction Study of Phase Transformation of Steel in Scuffing Process, Tribology Letters 57 (1) (2015) 6. doi:10.1007/s11249-014-0443-8.
URL https://doi.org/10.1007/s11249-014-0443-8

[21] T. Izumi, K. Yagi, J. Koyamachi, K. Saito, S. Sanda, S. Yamaguchi, H. Ikehata, Y. Yogo, J. Sugimura, Surface Deteriorations During Scuffing Process of Steel and Analysis of Their Contribution to Wear Using In Situ Synchrotron X-Ray Diffraction and Optical Observations, Tribology

Letters 66 (3) (2018) 120. doi:10.1007/s11249-018-1062-6.
URL https://doi.org/10.1007/s11249-018-1062-6
[22] K. Yagi, T. Izumi, J. Koyamachi, S. Sanda, S. Yamaguchi, K. Satio, M. Tohyama, J. Sugimura, In Situ Observation of Crystal Grain Orientation During Scuffing Process of Steel Surface Using Synchrotron X-ray Diffraction, Tribology Letters 68 (4) (2020) 115. doi:10.1007/s11249-020-01357-y.
URL https://doi.org/10.1007/s11249-020-01357-y
[23] T. Ungár, A. Borbély, The effect of dislocation contrast on x-ray line broadening: A new approach to line profile analysis, Applied Physics Letters 69 (21) (1996) 3173–3175. doi:10.1063/1.117951.
URL http://aip.scitation.org/doi/10.1063/1.117951
[24] T. Ungár, J. Gubicza, P. Hanák, I. Alexandrov, Densities and character of dislocations and size-distribution of subgrains in deformed metals by X-ray diffraction profile analysis, Materials Science and Engineering: A 319-321 (2001) 274–278. doi:10.1016/S0921-5093(01)01025-5.
URL https://linkinghub.elsevier.com/retrieve/pii/S0921509301010255
[25] M. A. Krivoglaz, Difraktsiya rentgenovskikh luchey i neytronov v neidealnykh kristallakh [Diffraction of X-rays and neutrons in imperfect crystals], Naukova Dumka, Kiev, 1983.
[26] T. Ungár, I. Dragomir, Á. Révész, A. Borbély, The contrast factors of dislocations in cubic crystals: the dislocation model of strain anisotropy in practice, Journal of Applied Crystallography 32 (5) (1999) 992–1002. doi:10.1107/S0021889899009334.
URL https://onlinelibrary.wiley.com/doi/10.1107/S0021889899009334
[27] I. C. Dragomir, T. Ungár, Contrast factors of dislocations in the hexagonal crystal system, Journal of Applied Crystallography 35 (5) (2002) 556–564. doi:10.1107/S0021889802009536.
URL https://onlinelibrary.wiley.com/doi/10.1107/S0021889802009536
[28] I. Bataev, D. Lazurenko, A. Bataev, V. Burov, I. Ivanov, K. Emurlaev, A. Smirnov, M. Rosenthal, M. Burghammer, D. Ivanov, K. Georgarakis, A. Ruktuev, T. Ogneva, A. Jorge, A novel operando approach to analyze the structural evolution of metallic materials during friction with application of synchrotron radiation, Acta Materialia 196 (2020) 355–369. doi:10.1016/j.actamat.2020.06.049.
URL http://www.sciencedirect.com/science/article/pii/S1359645420304845
[29] A. A. Bataev, V. G. Burov, A. A. Nikulina, I. A. Bataev, D. V. Lazurenko, A. I. Popelukh, D. A. Ivanov, A Novel Device for Quasi In Situ Studies of Materials Microstructure during Friction, Materials Performance and Characterization 7 (3) (2018) 20170065. doi:10.1520/MPC20170065.
URL http://www.astm.org/doiLink.cgi?MPC20170065
[30] S. C. Lim, M. F. Ashby, Overview no. 55 Wear-Mechanism maps, Acta Metallurgica 35 (1987) 1–24. doi:10.1016/0001-6160(87)90209-4.
[31] M. Ashby, S. Lim, Wear-mechanism maps, Scripta Metallurgica et Materialia 24 (5) (1990) 805–810. doi:10.1016/0956-716X(90)90116-X.
URL https://linkinghub.elsevier.com/retrieve/pii/0956716X9090116X
[32] M. F. Ashby, J. Abulawi, H. S. Kong, Temperature maps for frictional heating in dry sliding, Tribology Transactions 34 (4) (1991) 577–582. doi:10.1080/10402009108982074.
[33] J. H. Hubbell, S. M. Seltzer, Tables of x-ray mass attenuation coefficients and mass energy-absorption coefficients 1 keV to 20 meV for elements z = 1 to 92 and 48 additional substances of dosimetric interest (1995).
URL https://www.osti.gov/biblio/76335
[34] M. Smaga, A. Boemke, T. Daniel, M. W. Klein, Metastability and fatigue behavior of austenitic stainless steels, MATEC Web of Conferences 165 (2018) 04010. doi:10.1051/matecconf/201816504010.
URL https://www.matec-conferences.org/10.1051/matecconf/201816504010
[35] M. She, X. Liu, G. He, The deformation-induced martensite and dynamic strain aging during cyclic deformation in AISI 321, Materials Research Express 6 (2) (2018) 026530. doi:10.1088/2053-1591/aad958.
URL https://stacks.iop.org/2053-1591/6/i=2/a=026530?key=crossref.4d2749a2db12d78c1ffac96e827b764c
[36] M. G. Shahri, S. R. Hosseini, M. Salehi, Formation of Nano/Ultrafine Grains in AISI 321 Stainless Steel Using Advanced Thermo-Mechanical Process, Acta Metallurgica Sinica (English Letters) 28 (4) (2015) 499–504. doi:10.1007/s40195-015-0225-9.
URL https://link.springer.com/10.1007/s40195-015-0225-9
[37] M. Ridlova, L. Hyspecka, F. Wenger, P. Ponthiaux, J. Galland, P. Kubecka, Strain-induced martensitic transformation in type 321 austenitic stainless steel, Journal de Physique IV (Proceedings) 112 (2003) 429–432. doi:10.1051/jp4:2003917.
URL https://www.edpsciences.org/10.1051/jp4:2003917
[38] A. F. Padilha, P. R. Rios, Decomposition of Austenite in Austenitic Stainless Steels, ISIJ International 42 (4) (2002) 325–327. doi:10.2355/isijinternational.42.325.
URL https://joi.jlc.jst.go.jp/JST.Journalarchive/isijinternational1989/42.325?from=CrossRef
[39] B. Warren, X-ray studies of deformed metals, Progress in Metal Physics 8 (1959) 147–202. doi:10.1016/0502-8205(59)90015-2.
URL https://linkinghub.elsevier.com/retrieve/pii/0502820559900152
[40] P. Heilmann, D. Rigney, An Energy Based Model of Friction and Its Application to Coated Systems, Wear 72 (1981) 195–217. doi:10.1016/0043-1648(81)90367-7.
[41] D. A. Rigney, J. E. Hammerberg, Unlubricated sliding behavior of metals, MRS Bulletin 23 (6) (1998) 32–36. doi:10.1557/S0883769400030608.
[42] O. I. Abdullah, J. Schlattmann, Temperature analysis of a pin-on-disc tribology test using experimental and numerical approaches, Friction 4 (2) (2016) 135–143. doi:10.1007/s40544-016-0110-1.
URL https://link.springer.com/10.1007/s40544-016-0110-1
[43] X. Wu, M. Yang, F. Yuan, L. Chen, Y. Zhu, Combining gradient structure and TRIP effect to produce austenite stainless steel with high strength and ductility, Acta Materialia 112 (2016) 337–346. doi:10.1016/j.actamat.2016.04.045.
URL https://linkinghub.elsevier.com/retrieve/pii/S1359645416303135
[44] B. B. He, B. Hu, H. W. Yen, G. J. Cheng, Z. K. Wang, H. W. Luo, M. X. Huang, High dislocation density–induced large ductility in deformed and partitioned steels, Science 357 (6355) (2017) 1029–1032. doi:10.1126/science.aan0177.

URL https://www.sciencemag.org/lookup/doi/10.1126/science.aan0177
[45] S. Tarasov, V. Rubtsov, A. Kolubaev, Subsurface shear instability and nanostructuring of metals in sliding, Wear 268 (1-2) (2010) 59–66. doi:10.1016/j.wear.2009.06.027.
URL https://linkinghub.elsevier.com/retrieve/pii/S0043164809004505
[46] O. Trushin, E. Granato, S. C. Ying, P. Salo, T. Ala-Nissila, Energetics and atomic mechanisms of dislocation nucleation in strained epitaxial layers, Physical Review B 68 (15) (2003) 155413. doi:10.1103/PhysRevB.68.155413.
URL https://link.aps.org/doi/10.1103/PhysRevB.68.155413
[47] A. H. Cottrell, B. A. Bilby, Dislocation Theory of Yielding and Strain Ageing of Iron, Proceedings of the Physical Society. Section A 62 (1) (1949) 49–62. doi:10.1088/0370-1298/62/1/308.
URL https://iopscience.iop.org/article/10.1088/0370-1298/62/1/308



https://dspace.org/

Friction-induced phase transformations and evolution of microstructure of austenitic stainless steel observed by operando synchrotron X-ray diffraction

Emurlaev, K.; Bataev, I.; Ivanov, I.; Lazurenko, D.; Burov, V. ...

2022-05-22
Elsevier
https://doi.org/10.1016/j.actamat.2022.118033
Emurlaev K, Bataev I, Ivanov I, et al., (2022) Friction-induced phase transformations and evolution of microstructure of austenitic stainless steel observed by operando synchrotron X-ray diffraction, Acta Materialia, Volume 234, August 2022, Article number 118033

Downloaded from a DSpace repository. https://dspace.org/